

Compressibility effects in a turbulent annular mixing layer. Part 2. Mixing of a passive scalar

By JONATHAN B. FREUND†, PARVIZ MOIN
AND SANJIVA K. LELE

Center for Turbulence Research, Stanford University, Stanford, CA 94305, USA

(Received 11 November 1997 and in revised form 21 March 2000)

The mixing of fuel and oxidizer in a mixing layer between high-speed streams is important in many applications, especially air-breathing propulsion systems. The details of this process in a turbulent annular mixing layer are studied with direct numerical simulation. Convective Mach numbers of the simulations range from $M_c = 0.1$ to $M_c = 1.8$. Visualizations of the scalar field show that at low Mach numbers large intrusions of nearly pure ambient or core fluid span the mixing region, whereas at higher Mach numbers these intrusions are suppressed. Increasing the Mach number is found to change the mixture fraction probability density function from non-marching to marching and the mixing efficiency from 0.5 at $M_c = 0.1$ to 0.67 at $M_c = 1.5$. Scalar concentration fluctuations and the axial velocity fluctuations become highly correlated as the Mach number increases and a suppressed role of pressure in the axial momentum equation is found to be responsible for this. Anisotropy of scalar flux increases with M_c , and is explained via the suppression of transverse turbulence lengthscale.

1. Introduction

The process by which reactants, once entrained into a turbulent mixing layer, are mixed at a molecular level by diffusive processes is critical to several technologies. There are essentially three steps which lead to the creation of reaction products in such a flow: entrainment of fuel and oxidizer into the growing mixing layer, the mixing of fuel and oxidizer at the molecular level, and the chemical reaction. These steps are discussed by Dimotakis (1991) who argues that since each step occurs at subsequent Lagrangian times, the product formation rate, δ_P/t , depends on three separate factors. Here, we adapt his formula for spatially growing layers to the present case of a temporally growing layer,

$$\frac{\delta_P}{t} = \frac{\delta_\xi}{t} \times \frac{\delta_M}{\delta_\xi} \times \frac{\delta_P}{\delta_M}, \quad (1.1)$$

where t is time. δ_ξ is a concentration thickness, defined as the 99% scalar thickness, and thus δ_ξ/t is essentially the growth of the layer. The growth of the mixing layer is the subject of a companion paper (Freund, Lele & Moin 2000) which examines how compressibility affects the growth rate. The fraction of fluid that is mixed at

† Present address: Mechanical and Aerospace Engineering, University of California, Los Angeles, USA.

the molecular level is δ_M/δ_ξ , where δ_M is a thickness based upon the amount of mixed fluid. Its precise definition is given in §4.5. The ratio δ_M/δ_ξ is called the mixing efficiency and is a focus of study in this paper. The final factor in (1.1) is the fraction of molecularly mixed fluid which has chemically reacted and δ_P is a product thickness. The present simulations do not include chemical reactions, and we can only estimate δ_P using an infinitely fast reaction rate model.

There have been several attempts to quantitatively measure the mixing of a passive scalar in compressible mixing layers. To make accurate measurements of mixedness, the smallest scale of concentration fluctuations in the flow must be resolved so that molecularly mixed fluid is distinguished from that which has merely been ‘stirred’. Fluid stirred to very small scales, but not molecularly mixed, is erroneously interpreted as being molecularly mixed if the measuring technique has insufficient resolution.

The required resolution of scalar concentration measurements is set by the Batchelor scale and, in experiments, this is typically estimated with $\lambda_B \propto Sc^{-0.5} \delta_\xi Re_{\delta_\xi}^{-0.75}$. Highly resolved measurements have suggested that the constant of proportionality, for purposes of differentiating mixed and stirred fluid, is around 25 (Dowling 1988; Dahm & Dimotakis 1990). Of course, this value is only a guideline and the influence of the molecular diffusivity increases continuously from a negligible level at large inviscid scales to dominant at lengthscales $\lambda_{B_0} \approx Sc^{-0.5} \delta_\xi Re_{\delta_\xi}^{-0.75}$. Taking the proportionality constant to be 25 implies that measurement volumes of size λ_B or smaller have negligible error owing to under-resolution of small scales.

The necessary resolutions of experiments with a measurement dimension L are generally quantified in terms of λ_{B_0} ; L/λ_{B_0} values for many experiments are listed by Karasso & Mungal (1996) and Clemens & Mungal (1995). These are typically 10–100 times too under-resolved and, at present, it is very difficult to make measurements with sufficient resolution owing to camera limitations and, even more restrictive, laser sheet thickness. Therefore, in most cases, experimenters must infer mixedness from product formation or fluorescence quenching measurements. Such measurements are insensitive to volume averaging owing to under-resolution (Koochesfahani & Dimotakis 1986; Karasso & Mungal 1996; Clemens & Paul 1995; Island 1997) and are able to provide mixing-efficiency results. However, they cannot provide full information about the mixing process such as the probability density function of concentration fluctuations across the layer. An experiment or simulation which has adequate resolution to determine scalar concentrations unambiguously may provide such information without difficulty.

Here, we review only studies that use resolution-independent methods. A primary motivation for these experiments has been to determine the effect of Reynolds number and Mach number upon the mixing efficiency. In incompressible gaseous free shear flow, the mixing efficiency has been measured to be 0.49 (Frieler & Dimotakis 1988). That is, about half of the fluid in the mixing layer is ‘pure’, being from one free stream or the other, while the other half has experienced molecular mixing between the two. Hall, Dimotakis & Rosemann (1991) used a resolution-independent H_2 – F_2 –NO chemical reaction to measure mixing efficiency in a compressible shear layer and found that it decreased to 0.31 at $M_c = 0.92$. Clemens & Paul (1995) used the rapid quenching of NO fluorescence by O_2 to measure mixing efficiency in the initial mixing layer of a round jet and found that it increased slightly with increasing Mach number: from 0.45 at $M_c = 0.35$ to 0.48 at $M_c = 0.82$. However, their data, if extrapolated to the incompressible limit, do not appear to match the observed 0.49 value of Frieler & Dimotakis (1988). They cite Reynolds-number effects as a possible cause for the discrepancy. Though their method involves no chemical reaction, the

technique has been named ‘cold chemistry’ because it mimics an extremely fast chemical reaction with zero heat release. Island (1997) performed extensive plane mixing-layer measurements with the same technique and concluded that mixing efficiency increases slightly with both compressibility and Reynolds number.

There are essentially two distinct approaches to modelling mixing processes in turbulent shear flows. There are those who believe that gradient diffusion can accurately model the average mixing process (see Bilger 1989) and those who do not (e.g. Broadwell & Breidenthal 1982; Broadwell & Mungal 1991; Dimotakis 1991). The standard method for the first approach, gradient diffusion modelling, is to calculate an eddy viscosity from a k - ε turbulence model and then use a turbulent Prandtl number (often $Pr_T \approx 0.7$) to calculate scalar transport (see discussion and references in Bilger 1989). This method is used because it is simple and can give acceptable answers, but, as Corrsin (1974) points out, unless the turbulent scales are significantly smaller than the scales over which the mean flow varies, this technique does not have a strong theoretical basis. Those who prefer the second approach point to the existence of large-flow structures as violating the criterion discussed by Corrsin, and experimental evidence suggests that fluid elements are entrained and moved unmixed through the layer by large structures in a manner not consistent with a diffusive processes. They propose models based on large-scale entrainment of fluid into the layer and incorporate a hierarchy of concentration scales to describe the mixing process (Broadwell & Breidenthal 1982; Broadwell & Mungal 1991; Dimotakis 1991).

The inclusion of compressibility effects into models of either type has been hindered by uncertainty in the underlying physical processes. As discussed in the review of experimental work above, it is beginning to appear that compressibility has little effect upon the mixing efficiency. However, the large structural changes in the mixing layer, as the convective Mach number increases, have definite implications for the extension of the large-structure-based mixing models.

The goal of the present work is to study compressibility effects on the mixing process, and, in particular to examine Mach number trends under otherwise the same flow conditions. We briefly document the flow and the direct numerical simulation methods used to study it in §2. The resolution of the scalar field is addressed in §3. Simulation results are presented and discussed in §4 and conclusions are reiterated in §5.

2. Preliminaries

Many of the details of the flow we consider, the governing equations, and the simulation techniques are outlined in Part 1 (Freund *et al.* 2000) and are given in full detail in (Freund *et al.* 1997). The flow is a streamwise periodic annular mixing layer which corresponds to the early development of a jet. The initial mean flow had a ‘top hat’ like velocity profile specified with a hyperbolic tangent function and the initial momentum thickness was $\delta_m \approx 0.08r_o$, where r_o is the initial shear-layer radius (or the jet radius). The momentum thickness in this geometry is defined

$$\delta_m = \int_0^\infty \frac{\bar{\rho}\bar{v}_x}{\rho_j U_j} \left(1 - \frac{\bar{v}_x}{U_j}\right) r \, dr. \quad (2.1)$$

The turbulence was initialized with velocity perturbations of random phase and prescribed spectrum. The amplitude of the initial fluctuations was such that

$$\overline{v'_x v'_x} + \overline{v'_r v'_r} + \overline{v'_\theta v'_\theta}^{1/2} = 0.05 U_{j_0}. \quad (2.2)$$

The compressible Navier–Stokes equations were solved numerically using sixth-order compact finite-difference and spectral methods to approximate spatial derivatives for all terms and fourth-order Runge–Kutta time advancement. The computational domain was cylindrical and extended to $21r_o$ in the axial direction and $3.5r_o$ in the radial direction. At $r = 3.5r_o$, non-reflecting characteristic boundary conditions were applied. The mesh had $448 \times 146 \times 192$ points in the axial, radial and azimuthal directions.

Nine cases were simulated at nearly the same flow conditions, with the exception of the centreline Mach number which varied from $M_j = 0.2$ to $M_j = 3.5$. The subscript $()_j$ indicates a centreline value. In this study, we focus on the point of flow development when the momentum thickness was $\delta_m = 0.2r_o$, which is before the potential core closes. Choosing such a point preserves geometrical similarity between the different cases and this choice is discussed in more detail by Freund *et al.* (1997, 1999) along with detailed analysis of the turbulence development. The convective Mach number is typically used to quantify compressibility and ranged from $M_c = 0.1$ to $M_c = 1.8$. The cases at $M_c = 0.2$ and $M_c = 0.99$ were simulated with 4 and 10 independent realizations, respectively, to increase the sample size with ensemble averaging. In all cases, the Reynolds number was $Re = \rho_j U_j r_o / \mu_j \approx 2300$ and the temperature ratio was $T_j / T_\infty = 1.12$. The Crocco–Busemann relation was used to prescribe the initial temperature profile and the initial pressure was uniform.

The mass, momentum and energy equations in cylindrical coordinates are discussed in Freund *et al.* (1997, 1999) and the reader is referred there for details. An advection–diffusion equation was solved simultaneously with the flow equations:

$$\frac{\partial}{\partial t}(\rho\xi) + \frac{\partial}{\partial x}(\rho\xi v_x) + \frac{1}{r} \frac{\partial}{\partial r}(r\rho\xi v_r) + \frac{1}{r} \frac{\partial}{\partial \theta}(\rho\xi v_\theta) = -\frac{\partial G_x}{\partial x} - \frac{1}{r} \frac{\partial r G_r}{\partial r} - \frac{1}{r} \frac{\partial G_\theta}{\partial \theta}, \quad (2.3)$$

where ξ represents a non-dimensional scalar concentration and G is a vector of the diffusive fluxes calculated with Fick’s law. The Schmidt number was unity in all the simulations ($Sc = 1$). The scalar concentration was normalized in terms of the dimensional centreline and ambient values, ξ_j and ξ_∞ , as

$$\xi = \frac{\xi^* - \xi_\infty}{\xi_j - \xi_\infty}, \quad (2.4)$$

where ξ^* is the ‘un-normalized’ concentration. Thus, the scalar concentration and mixture fraction are the same, and these terms are used interchangeably throughout this paper. The initial condition for the scalar concentration was

$$\xi(r) = \frac{\bar{u}(r)}{U_{j_0}} = \frac{1}{2} \left[1 - \tanh \left[\frac{1}{4b} \left(\frac{r}{r_o} - \frac{r_o}{r} \right) \right] \right], \quad (2.5)$$

where b is a thickness parameter equal to 0.08 in all cases.

3. Resolution of the scalar field

To estimate the ‘best case’ resolution of the present simulations in a manner that can be compared with experiments, we calculate L/λ_{B_0} values using the mesh spacing as the measurement length, L . Worst-case values in the three coordinate directions are

$$\frac{\Delta x}{\lambda_{B_0}} = 17, \quad \frac{\Delta r}{\lambda_{B_0}} = 10, \quad \frac{r\Delta\theta}{\lambda_{B_0}} = 21, \quad (3.1)$$

and are based on $Re_{\delta_\xi} \approx 3900$ and the 99% scalar-layer thickness $\delta_\xi = 1.7r_o$ which corresponds to momentum thickness $\delta_m = 0.2r_o$.

However, we are not at liberty, as experimentalists are, to assume that the simulated flow is correct, even if the grid spacing has this resolution. It is conceivable that scales smaller than in (3.1) have some influence on the flow field which is not captured. Fortunately, more precise measures of the resolution are available by calculating the dissipating scales and by examining scalar concentration and dissipation spectra.

For $Sc = 1$, the spectra of both kinetic energy and scalar fluctuations fall off sharply near the Kolmogorov scale, $\lambda_K = (\nu^2/\varepsilon)^{1/4}$ (Batchelor 1957), where ν is the kinematic viscosity and ε is the dissipation rate of turbulent kinetic energy. We use ε to calculate values for the Batchelor scale ($\lambda_B = \lambda_K$ for $Sc = 1$) in order to provide a more direct measure of the resolution. Of course, ε also depends upon the resolution and therefore can also be underresolved. However, calculating ε using only every other mesh point changed its value by less than 10% and we concluded that it is sufficiently accurate. The worst case for $\Delta x/\lambda_B$ varied from a value of 3.1 at $M_c = 0.2$ to 2.4 at $M_c = 1.80$, the worst case for $r\Delta\theta/\lambda_B$ was approximately 2.3 for all cases, and the worst case for $\Delta r/\lambda_B$ varied from 1.1 to 0.7 with increasing M_c .

Perhaps the best way of quantifying the scalar resolution is by simply examining spectra of ζ' and the scalar dissipation. Spectra for the $M_c = 0.21, 0.99$, and 1.80 cases, which are typical of the low-, middle-, and high-speed flows, respectively, are plotted in figure 1. The $M_c = 0.21$ case was selected over the $M_c = 0.1$ case, because it had 4 realizations available for ensemble averaging. Ensemble averaging was also used for the $M_c = 0.99$ case, but only one realization was available for the $M_c = 1.80$ case. Owing to the well-known limitations of direct numerical simulations, the Reynolds number (as well as $ReSc$) must necessarily be low, and this manifests itself in very limited or non-existent 'inertial' ranges. Similarly, short inertial ranges are apparent in the low-Reynolds-number experimental data of Dowling & Dimotakis (1990) who examined the dissipation portion of the spectrum in a fully developed jet. All the axial one-dimensional spectra (figure 1a) have a short region of slope $-\frac{5}{3}$, and at the end of this region, on the high wavenumber side, the onset of significant diffusive effects can be observed. For the azimuthal spectra (figure 1b), only the $M_c = 0.21$ case has a region of $-\frac{5}{3}$ slope. In all cases, the spectra drop by over two orders of magnitude after molecular diffusion effects become evident. The very highest wavenumbers in the simulations show anomalous behaviour, but the energy is so low at this wavenumber that the influence on the mixing data is negligible. Minor under-resolution and the modified wavenumber of the sixth-order Padé scheme may be responsible for high-wavenumber behaviour of the x -spectra. The 'up-turn' at the high-wavenumber end of the θ -spectra has also been observed by Moin *et al.* (1991) and was attributed to aliasing errors. The flat region in the high-wavenumber end of the $M_c = 1.80$ axial spectrum is believed to be due to poor resolution of eddy shocklets. These occupy a very small portion of the flow volume and are not dynamically significant (Freund *et al.* 2000). We also note that the suspicious flat region has 10^4 times lower 'energy' content than the highest portion, and therefore is not likely to degrade the overall solution.

As a final measure of the scalar field resolution, we examine scalar dissipation spectra. Each term in the scalar dissipation,

$$\varepsilon_\xi = G'_x \frac{\partial \xi'}{\partial x} + G'_r \frac{\partial \xi'}{\partial r} + G'_\theta \frac{1}{r} \frac{\partial \xi'}{\partial \theta}, \quad (3.2)$$

is sensitive to the resolution of the scalar field in the direction in which the derivatives

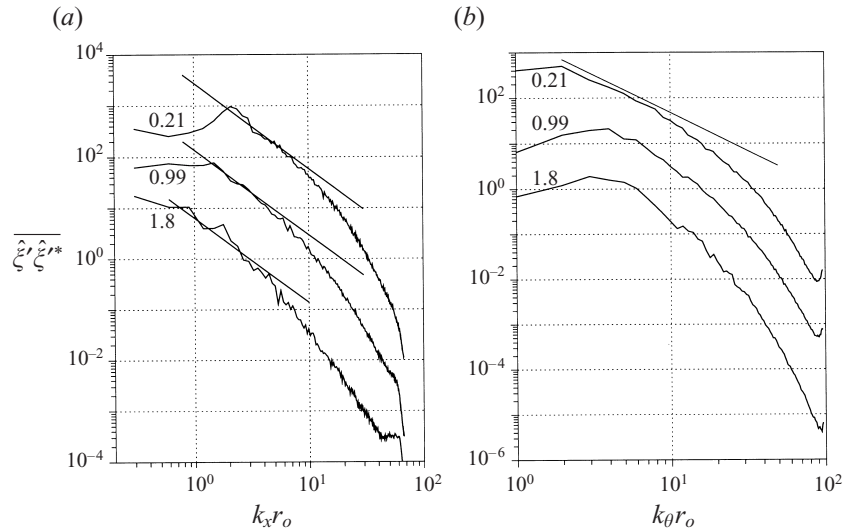


FIGURE 1. One-dimensional (a) axial and (b) azimuthal spectra of ξ' at $r = r_o$ and $\delta_m = 0.2r_o$. The numbers indicate the convective Mach numbers of the different cases. The straight lines have slope $-\frac{5}{3}$ and the $M_c = 0.99$ and $M_c = 1.80$ curves have been divided by 10 and 100, respectively.

are taken. If we assume constant fluid properties, the spectral representation of the first term in (3.2) is proportional to $k_x^2 \hat{\xi}' \hat{\xi}'^*$, where k_x is the axial wavenumber, $\hat{\xi}'$ is the Fourier transformed scalar concentration perturbation field, and the * indicates complex conjugate. This quantity is plotted in figure 2(a) for the $M_c = 0.21, 0.99$ and 1.80 cases. The dissipation clearly rises in the low wavenumbers and then drops at the highest wavenumbers. There is a small bump evident at high wavenumbers for the $M_c = 1.80$ case. Again, this is believed to be due to the shocklets discussed above. It is clear that we are capturing nearly all of the scalar dissipation in the simulations, and we conclude that the smallest significant scales are resolved. The same is true in the azimuthal direction (figure 2b). Since the flow is inhomogeneous in the radial direction, radial spectra cannot be calculated. However, it is clear from the other estimates of resolution discussed earlier that the radial direction is the best resolved.

4. Results and discussion

This section documents and provides a discussion of the results from the simulations. In §4.1, the development of the mean scalar profile is presented, and in §4.2 we visualize instantaneous scalar fields with grey-scale images. Probability density functions (p.d.f.s) of mixture fraction are discussed in §4.3, the radial scalar correlation lengthscale is computed and discussed in §4.4, and the mixture fraction p.d.f.s are used to calculate mixing efficiency in §4.5. In §4.6, we study scalar fluxes and velocity-concentration correlations, and in §4.7, we examine the structure of the scalar field with visualizations and joint p.d.f.s of velocity and scalar concentration. Joint p.d.f. results are useful for the development of diffusion flame models (Bilger 1989).

4.1. Mean passive scalar

The mean passive scalar evolution is nearly identical to the mean velocity evolution which is expected based upon self-similarity arguments and the nature of the momentum and scalar equations, and unity Schmidt number. The passive scalar

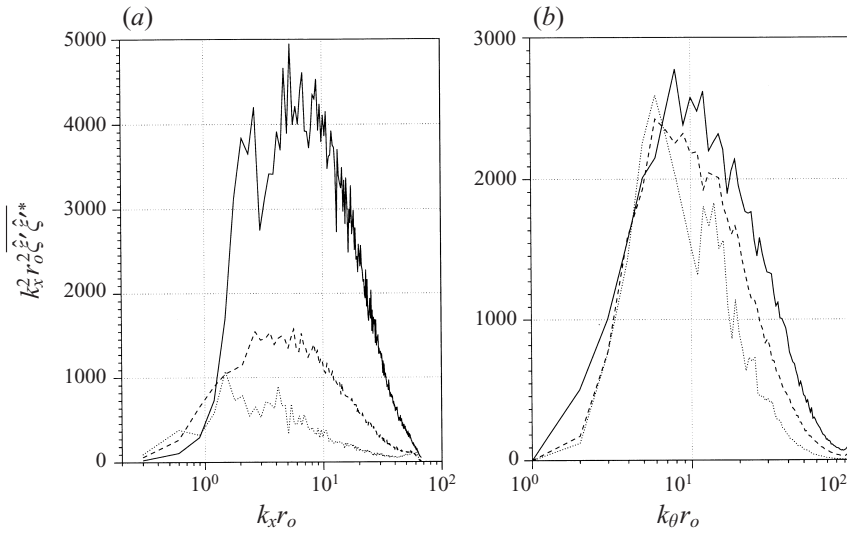


FIGURE 2. One-dimensional (a) axial and (b) azimuthal dissipation spectra at $r = r_o$: —, $M_c = 0.21$; ----, $M_c = 0.99$; ····, $M_c = 1.80$.

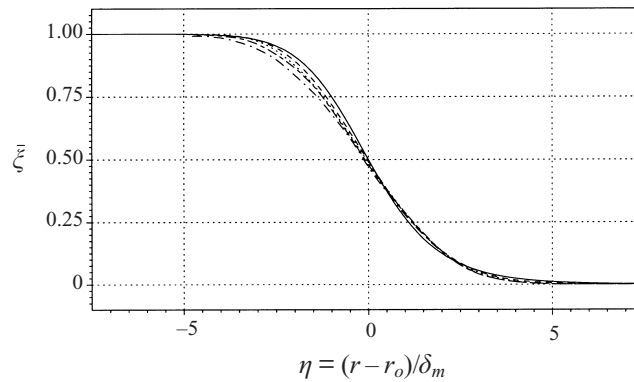


FIGURE 3. Self-similar like collapse of mean passive scalar concentration data for $M_c = 0.99$: —, $tU_{jo}/r_o = 0.0$; ----, 4.1; ····, 8.1; —·—, 12.2; — — —, 16.3.

concentration is plotted against a similarity variable, $\eta = (r - r_o)/\delta_m$, in figure 3 for the $M_c = 0.99$ case. The collapse is good considering that the flow is not formally self-similar and is nearly identical to the collapse of the mean velocity profiles (see Freund *et al.* 1997, 2000). The other cases show a similar evolution, and there are no observable trends in the ‘self-similar’ profile shapes with increasing Mach number.

4.2. Scalar field visualizations

Grey-scale images of scalar concentration at $\delta_m = 0.2r_o$ for the $M_c = 0.21$, $M_c = 0.99$ and $M_c = 1.80$ cases are shown in figures 4 to 6. These are similar to images produced in experimental studies of compressible mixing layers (Clemens & Mungal 1995; Messersmith & Dutton 1996; Papamoschou & Bunyajitradulya 1997). As in Clemens & Mungal (1995), the low-speed flow (side view, figure 4) appears dominated by large structures which drive deep intrusions of ambient fluid into the core and pull core fluid into the ambient. The $M_c = 0.99$ flow (side view, figure 5) shows similar signs of

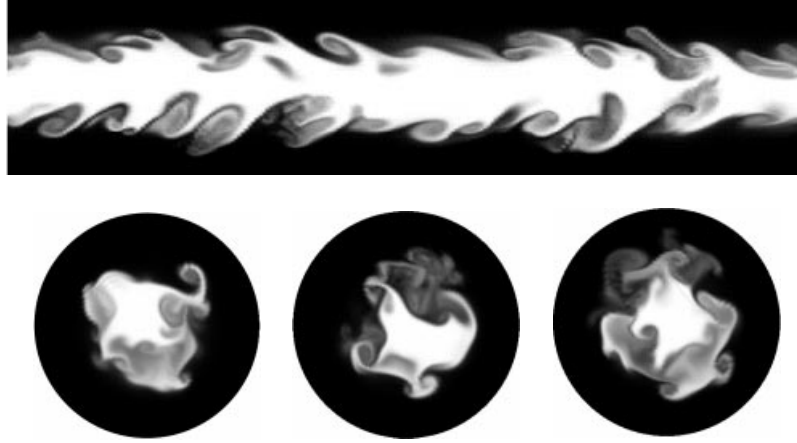


FIGURE 4. Passive scalar concentration in the $M_c = 0.21$ mixing layer at $\delta_m = 0.2r_o$. Black is pure ambient fluid and white is pure interior fluid. The end views are from $x = \frac{1}{3}L_x, \frac{2}{3}L_x,$ and L_x .

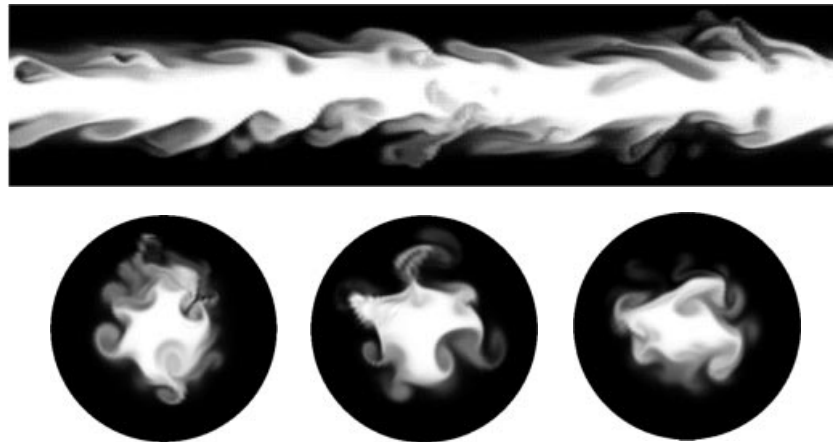


FIGURE 5. Passive scalar concentration in the $M_c = 0.99$ mixing layer at $\delta_m = 0.2r_o$. Black is pure ambient fluid and white is pure interior fluid. The end views are from $x = \frac{1}{3}L_x, \frac{2}{3}L_x,$ and L_x .

these structures, but they are less prevalent and do not cause such deep penetrations across the mixing region. A similar suppression with increasing Mach number was observed by Clemens & Mungal (1995). There is no evidence of these structures in the $M_j = 1.80$ case (side view, figure 6) and there are no associated fluid intrusions.

The end views in figures 4 to 6 are remarkably similar, given the very different nature of the side views. There is perhaps more mixed fluid (grey) in the higher-Mach-number cases, but the structures appear remarkably similar. In all cases, there is evidence that counter-rotating streamwise vortices expel jet fluid as mushroom shaped ejection into the ambient flow. Similar structures have been observed in subsonic jets by Liepmann & Gharib (1992) and Fatica, Verzicco & Orlandi (1994).

4.3. Mixture fraction probability density functions

P.d.fs of mixture fraction, calculated using 26 bins, are shown in figure 7 for the $M_c = 0.21, 0.99$ and 1.80 cases at the $\delta_m = 0.2r_o$ point of layer development. These cases were selected to represent the changes that occur in the flow with increasing

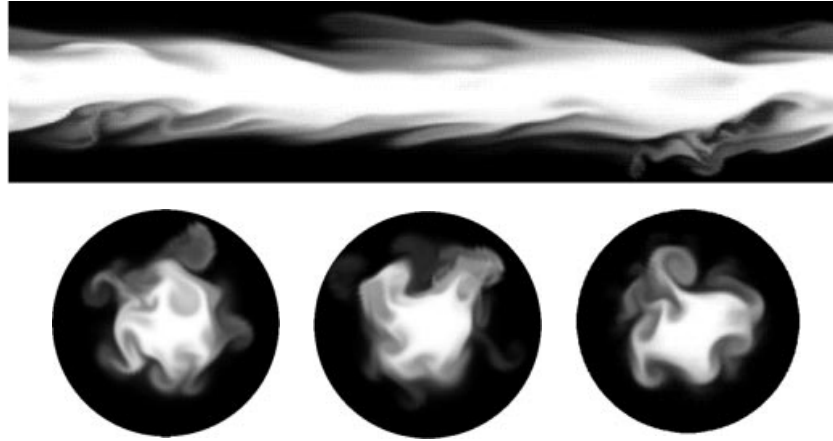


FIGURE 6. Passive scalar concentration in the $M_c = 1.80$ mixing layer at $\delta_m = 0.2r_o$. Black is pure ambient fluid and white is pure interior fluid. The end views are from $x = \frac{1}{3}L_x$, $\frac{2}{3}L_x$, and L_x .

Mach number. Again, the $M_c = 0.21$ case was chosen over the $M_c = 0.1$ case because 4 realizations were available. Ensemble averaging was also used for the $M_c = 0.99$ case. The $M_c = 1.80$ case has a more ‘jagged’ appearance because only one realization was available.

In all cases, the initial condition for the scalar was a laminar profile (no perturbations), and so the initial p.d.f. was a delta function that moved (marched) monotonically from one pure stream to the other as a function of the radial location. The $M_c = 0.21$ p.d.f. (figure 7a) has developed from its initial marching form, into a non-marching form and the most probable scalar concentration jumps discontinuously from $\xi = 1$ to $\xi = 0$ with increasing r . The behaviour in figure 7(a) is qualitatively similar to p.d.f.s observed in incompressible or nearly incompressible experiments (Konrad 1976; Koochesfahani & Dimotakis 1986; Frieler 1992; Karasso & Mungal 1996). Though most experimental measurements of p.d.f.s are unreliable owing to poor resolution (Koochesfahani & Dimotakis 1986; Karasso & Mungal 1996), measured p.d.f.s typically have a more distinct bump at a concentration midway between the pure concentrations.

Karasso & Mungal (1996) have concluded, based upon indirect evidence and p.d.f.s inferred by others with resolution-free methods (Frieler 1992), that after the layer has undergone three vortex pairings, the true incompressible p.d.f. should change from a non-marching type to a ‘tilted’ type, where the bump at an intermediate mixture fraction is biased toward the mean concentration. They estimated the three vortex pairing point based upon initial shear layer instability modes. The central bump in figure 7(a) is not distinct enough to draw any conclusions about non-marching versus tilted behaviour, and it is not clear that the same rule should apply to the annular mixing layer.

In a time-developing incompressible plane mixing-layer simulation, Rogers & Moser (1994) observed both marching and non-marching p.d.f.s depending upon the initial conditions. Their layer with the largest initial forcing developed large roller structures and braid regions and had a non-marching mixture fraction p.d.f. They proposed that pure fluid engulfed by the large structures caused the observed p.d.f. behaviour. Our p.d.f. for the $M_c = 0.21$ simulations is similar to their most highly forced case and so we adopt their conclusion that large structures are responsible for engulfing significant

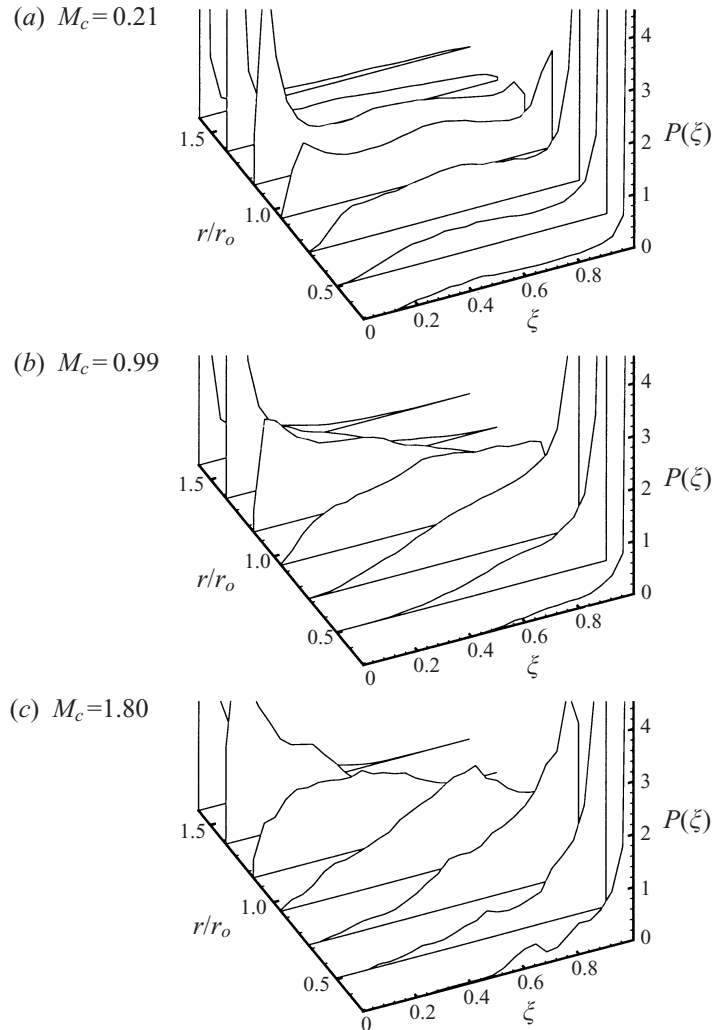


FIGURE 7. Probability density function of scalar concentration.

amounts of pure fluid into the low-Mach-number mixing layer. In the middle of their mixing region, they too observe a less distinct bump at an intermediate mixture fraction than is observed experimentally, though their bump is more distinct than ours.

At $M_c = 0.99$ (figure 7b) the p.d.f. has switched from non-marching to marching, and the most probable concentration now moves monotonically across the layer. This behaviour is consistent with decreasing engulfment of pure fluid by large structures (Rogers & Moser 1994) and may be associated with the change from azimuthally correlated to more streamwise oriented structures that occurs in the flow (Freund *et al.* 2000) which is also predicted by linear stability analysis for plane mixing layers (Sandham & Reynolds 1991). Large structures are also less prevalent in flow visualizations (figures 4 and 5). Concentration p.d.f.s reported in the literature at approximately the same Mach number are also marching (Clemens & Mungal 1995; Clemens & Paul 1995), but are unreliable owing to inadequate resolution.

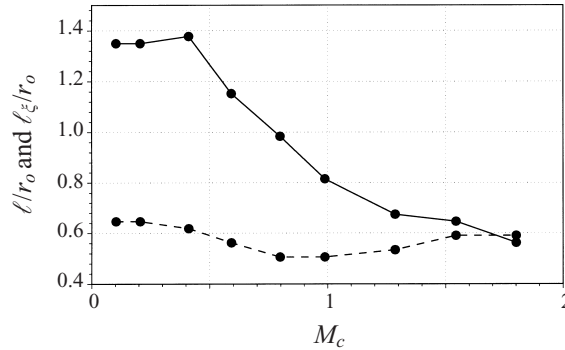


FIGURE 8. Transverse lengthscales defined in (4.1) and (4.2): —, ℓ ; - - - - , ℓ_ξ .

No attempt has been made to measure the p.d.f. experimentally at a Mach number as high as $M_c = 1.8$. We see in figure 7(c) that the marching behaviour has become more pronounced with a sharper peak moving across the layer, which is consistent with still less participation of large structures engulfing fluid into the layer.

4.4. Transverse scalar fluctuation lengthscale

Despite the obvious change seen in the structure of the layer both in the visualizations and in the concentration p.d.f.s, the transverse correlation length of the scalar fluctuations, ℓ_ξ , defined by

$$\frac{\overline{\xi'(r_o - \ell_\xi/2)\xi'(r_o + \ell_\xi/2)}}{\overline{\xi'(r_o)\xi'(r_o)}} = 0.1, \quad (4.1)$$

remains surprisingly constant with increasing Mach number. This definition is analogous to the radial turbulence lengthscale, ℓ , defined by

$$\frac{\overline{v'_r(r_o - \ell/2)v'_r(r_o + \ell/2)}}{\overline{v'_r(r_o)v'_r(r_o)}} = 0.1, \quad (4.2)$$

that was discussed at length in Part 1. Both these lengthscales are shown in figure 8. While ℓ is suppressed by over a factor of two between the lowest and highest Mach numbers, ℓ_ξ is approximately $0.6r_o$, regardless of Mach number. The apparently contradictory behaviour, however, can be explained as follows. While the deep intrusions seen in the low-Mach-number flows in figure 4 should indeed increase the radial scalar lengthscale relative to higher-Mach-number flows, these same structures also appear to wind the fluid back upon itself. The ‘folds’ and ‘spirals’ created by this action will decrease the correlation length ℓ_ξ . In this particular flow, these two effects appear to balance one another.

The most important implication of this behaviour is that a radial lengthscale estimated from a passive scalar field can be misleading, both with regard to the dynamic lengthscales of the flow and the process by which fluid is mixed. Given only the scalar correlation length, it might be inferred that the transverse turbulence structures do not change with M_c , while all the other evidence we have examined suggests that it changes significantly. Similarly, this radial lengthscale is shorter than that obtained with the more dynamically relevant radial velocity fluctuations. This might motivate diffusion modelling of transport when it may not be justified according to the lengthscale criterion discussed in § 1.

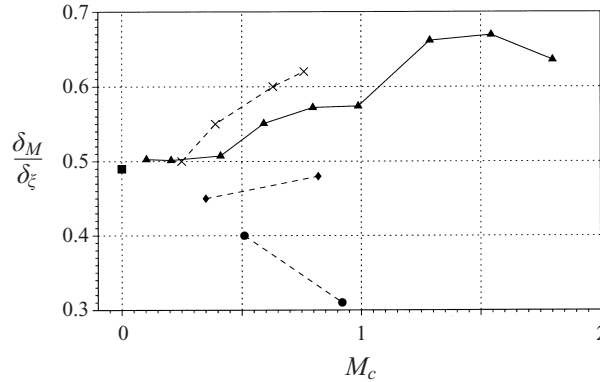


FIGURE 9. Mixing efficiency as defined in (4.3) for \blacktriangle , the present simulations; \times , Island 1997; \blacklozenge , Clemens & Paul 1995; \bullet , Hall *et al.* 1991; \blacksquare , Frieler & Dimotakis 1988.

4.5. Mixing efficiency

The mixing efficiency is defined as the fraction of the fluid in the layer that has been mixed at the molecular level. If a fast chemical reaction occurs, the mixing efficiency can be inferred from the formation of product. However, in the present simulations we do not have such a direct measure, and we define the mixing efficiency in terms of mixture fraction p.d.f.

$$\frac{\delta_M}{\delta_\varepsilon} = \frac{1}{\delta_\varepsilon} \int_0^\infty \int_\varepsilon^{1-\varepsilon} P(\zeta, r) d\zeta r dr. \quad (4.3)$$

Note that the infinite upper bound on the integral is equivalent to $3.5r_o$, the radial extent of the computational domain, because $\zeta = 0$ beyond this point. All experimental and computational data have noise which necessitates the definition of pure fluid to be within ε of $\zeta = 1$ or $\zeta = 0$. Equivalently, we could use an infinitely fast reaction rate model. Setting the stoichiometric mixture fraction to be first $\zeta_o = \varepsilon$ and then $\zeta_o = 1 - \varepsilon$ we could infer the mixing efficiency in the same manner as in ‘flip’ experiments (Koochesfahani & Dimotakis 1986; Karasso & Mungal 1996) where direct measurement of the p.d.f. was not possible. The choice of ε is somewhat arbitrary and does influence the resulting mixing efficiency. An increase in ε will decrease the amount of fluid that is considered mixed, while decreasing it will have the opposite effect. Choices for ε in experimental studies have been made, both for convenience and for reasons based on experimental limitations. Koochesfahani & Dimotakis (1986) collected their data into 32 bins for estimating their p.d.f.s and took $\varepsilon = 0.031$, which corresponds to defining all the fluid in the extreme bins to be pure. Clemens & Paul (1995) used $\varepsilon = 0.1$, which, given the signal-to-noise ratio of their measurements, was necessary to yield zero probability of mixed fluid in the free streams. Our p.d.f.s were calculated using 26 bins, but they were constructed so that the first and last bins were centred on the values of $\zeta = 0$ and $\zeta = 1$, respectively. Using only the extreme bins to represent pure fluid gives $\varepsilon = 0.02$. Less than 1 in 2.5×10^5 mesh points had ζ values that fell into bins outside the physically realizable range $\zeta = 0 \rightarrow 1$. Using $\varepsilon = 0.06$ drops the mixing efficiency by approximately 0.1 at all Mach numbers, but leaves the Mach number trend unchanged.

Mixing efficiency results are plotted in figure 9. There is a clear increasing trend from 0.5 at $M_c = 0.1$ to 0.67 at $M_c = 1.54$. The highest-Mach-number case, $M_c = 1.8$, shows a decrease in mixing efficiency. The reasons for this are unclear and more

simulations at high Mach number are needed to determine the cause. The mixing-layer growth rate suppression does appear to saturate at this Mach number, which may be related to this anomalous behaviour. The low-Mach-number simulations, for the chosen values of ε , agree very well with the incompressible point of Frieler & Dimotakis (1988). The present study also agrees fairly well with the data of Island (1997).

The increase in mixing efficiency with increasing Mach number is somewhat slower for our data than that of Island (1997), but the difference may be caused by the geometrical difference between the two flows. This is consistent with growth rates and Reynolds stresses which also show the effects of compressibility more slowly than plane mixing layers (Freund *et al.* 2000). However, Island (1997) attributes his increase in $\delta_M/\delta_\varepsilon$ more to increasing Reynolds number than Mach number. The present direct simulation results have lower Reynolds number than his by a factor of about 100, but they are all at nearly the same Reynolds number.

The slope of our data agrees better with that of Clemens & Paul (1995) who study a round jet mixing layer. However, they claim, citing the work of Mungal *et al.* (1985), that if Reynolds number effects were taken into account they would have a less significant increase in mixing efficiency at higher Mach number. More recently, however, finite rate chemistry effects have been attributed to the observed Reynolds number effect in Mungal, Hermanson & Dimotakis (1985) (Mungal 1997, private communication). Magnitude comparisons are weak because of the dependence upon ε , but Clemens & Paul (1995) point out that their quenching method may overestimate the amount of pure fluid by 5%–10% which would bring their data into better agreement with our data for $\varepsilon = 0.02$. The data of Hall *et al.* (1991) clearly disagrees in both trend and magnitude with all the other data. More data are needed before any consensus will be reached concerning the amplitude and the relative importance of Re and M . However, both the present simulation and experiments using NO–O₂ quenching show slowly increasing mixing efficiency with increasing Mach number.

Though no chemical reactions were simulated, the amount of product formed may be estimated with an infinite-reaction-rate, zero-heat-release model. For a stoichiometric mixture fraction ξ_o , the reaction factor in (1.1) is then

$$\frac{\delta_P}{\delta_M} = \frac{1}{\delta_M} \int_0^\infty \min\left(\frac{\xi}{\xi_o}, \frac{1-\xi}{1-\xi_o}\right) r \, dr. \quad (4.4)$$

This is plotted for three different ξ_o in figure 10. The fraction of mixed fluid which has reacted is essentially constant with Mach number for each stoichiometric ratio and is only a weak function of ξ_o . Under the assumptions of the infinite-reaction-rate model, it is clear that the mixing efficiency and especially the growth rate are the dominant factors in (1.1) that influence the product-formation rate. However, finite-rate chemistry effects would almost certainly cause δ_P/δ_M to depend upon the Mach number. If a chemical reaction were to occur in these flows, its Damköhler number would decrease by a factor of 17 between the lowest and highest Mach numbers.

4.6. Statistics of scalar concentration

In presenting statistical data we must decide whether Favre or Reynolds averages are the most relevant. When modelling transport, expressions are simplified if Favre averages are used, and for this reason we provide Favre-averaged fluxes. However, when examining correlation coefficients, we quantify the similarity of scalar concentration perturbations to velocity perturbations, and, therefore, the Reynolds average is the most appropriate vehicle to show this. Mixture fraction r.m.s. values are also

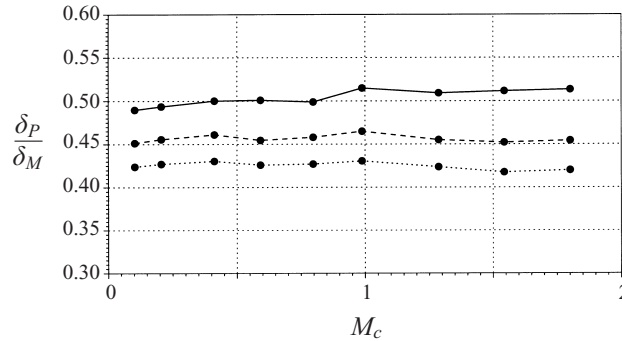


FIGURE 10. Product fraction assuming infinite-rate chemistry for stoichiometric mixture fraction: —, $\xi_o = 0.25$; ----, 0.50; ····, 0.75.

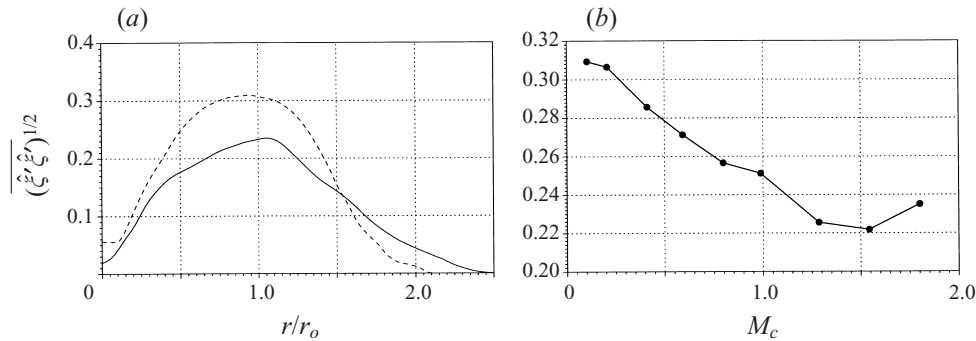


FIGURE 11. Root-mean-squared scalar concentration fluctuations at $\delta_m = 0.2r_o$. (a) Radial profiles for ----, $M_c = 0.2$ and —, $M_c = 1.8$; (b) peak values for all the cases.

presented as Reynolds averages, which are easier to compare with experiments. The differences between Favre- and Reynolds-averages are small. All trends are the same regardless of which is used.

Root-mean-squared (r.m.s.) concentration fluctuations for the lowest and highest Mach numbers ($M_c = 0.2$ and $M_c = 1.8$) are plotted in figure 11(a). The curves at all Mach numbers have similar shapes. The maximum values are plotted in figure 11(b). The values are higher than those measured by Clemens & Paul (1995), but under-resolution of those measurements may explain this difference. Nonetheless, higher peak values of scalar r.m.s. are consistent with higher Reynolds stresses in the simulations relative to experimentally measured values for plane mixing layers (Freund *et al.* 2000). This difference was attributed to geometrical differences and the associated lack of a self-similar development. The Clemens & Paul (1995) results are from a round jet mixing layer, but its δ_ξ/r_o is smaller than in the present case.

Because radial profiles of the scalar fluxes are, like the scalar r.m.s. profiles, very similar at different Mach numbers, we provide the full profiles only for the extreme cases (figure 12a) and plot the maximum values as a function of Mach number (figure 12b). As with the Reynolds stresses (Freund *et al.* 2000), the axial component ($\overline{\rho v_x'' \xi''}$) remains constant, when normalized by the centreline mean velocity, while the radial component ($\overline{\rho v_r'' \xi''}$) is highly suppressed from the lowest to highest Mach number cases. The peak of the $\overline{\rho v_x'' \xi''}$ flux is significantly sharper in the $M_c = 1.8$ case, but this is not believed to be statistically significant. At the higher Mach numbers, the

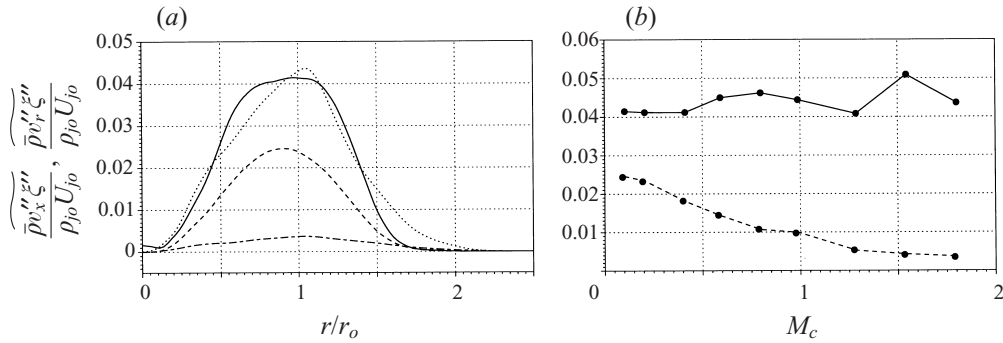


FIGURE 12. Turbulent passive scalar fluxes. (a) $M_c = 0.2$: —, $\overline{\rho v_x'' \xi''} / \rho_{j_0} U_{j_0}$; ----, $\overline{\rho v_r'' \xi''} / \rho_{j_0} U_{j_0}$; $M_c = 1.8$: ····, $\overline{\rho v_x'' \xi''} / \rho_{j_0} U_{j_0}$; - · - ·, $\overline{\rho v_r'' \xi''} / \rho_{j_0} U_{j_0}$. (b) —, Peak $\overline{\rho v_x'' \xi''} / \rho_{j_0} U_{j_0}$; ----, peak $\overline{\rho v_r'' \xi''} / \rho_{j_0} U_{j_0}$.

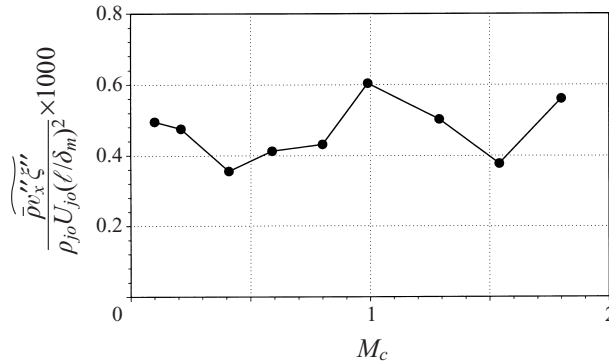


FIGURE 13. Radial velocity flux scaled by the transverse turbulence lengthscale.

sample size for averaging becomes smaller owing to the fact that there are fewer large structures in the axial domain. In figure 12(b), the peak in $\overline{\rho v_x'' \xi''}$ flux remains nearly constant, but the peak in $\overline{\rho v_r'' \xi''}$ flux is suppressed by nearly a factor of 7 between the lowest and highest Mach numbers.

In Part 1 of this study, it was shown that the transverse turbulence correlation length ℓ defined in (4.2) was successful at scaling the Reynolds stresses. In particular, $\overline{v_x' v_r'} / U_j^2 (\ell / \delta_m)^2$ and $\overline{v_r' v_r'} / U_j^2 (\ell / \delta_m)^2$ were nearly constant with increasing Mach number. Figure 13 shows that scaling by $(\ell / \delta_m)^2$ also removes the strong Mach-number dependence of $\overline{\rho v_r'' \xi''} / \rho_{j_0} U_{j_0}$. This scaling should not be a surprise given its success for scaling $\overline{v_x' v_r'}$ and the strong correlation between the axial velocity and scalar fluctuations which is shown next.

Correlation coefficients are given in figures 14–16. $\overline{v_x' \xi'} / v_{x,rms}' \xi'_{rms}$ is plotted for the $M_c = 0.2, 0.99$ and 1.8 cases in figure 14(a). It is nearly constant across the middle of the mixing region and tends to drop near the edges. However, its numerator and denominator both become small in the edge regions, making it a poorly behaved quantity from which it is difficult to draw conclusions. It is clear that the axial velocity and scalar concentration fluctuations become highly correlated as the Mach number increases. This trend is also apparent in figure 14(b), which shows the correlation at

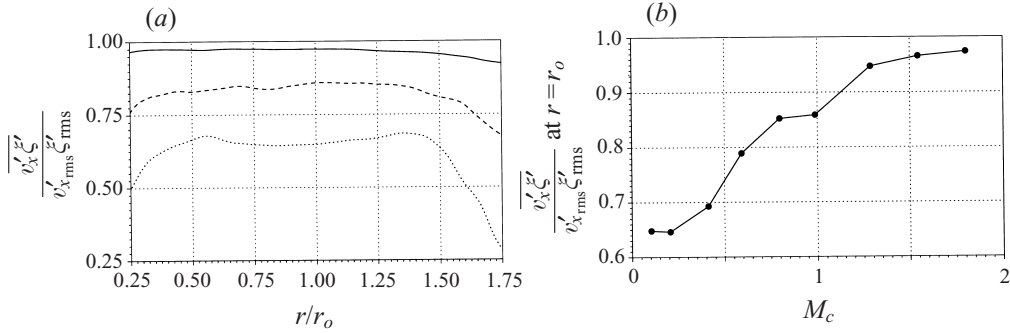


FIGURE 14. Correlation coefficient between axial velocity and scalar concentration fluctuations. (a) $\cdots\cdots$, $M_c = 0.2$; $-\cdots-$, $M_c = 0.99$; $—$, $M_c = 1.8$. (b) Correlation coefficient for all Mach number cases at $r = r_o$.

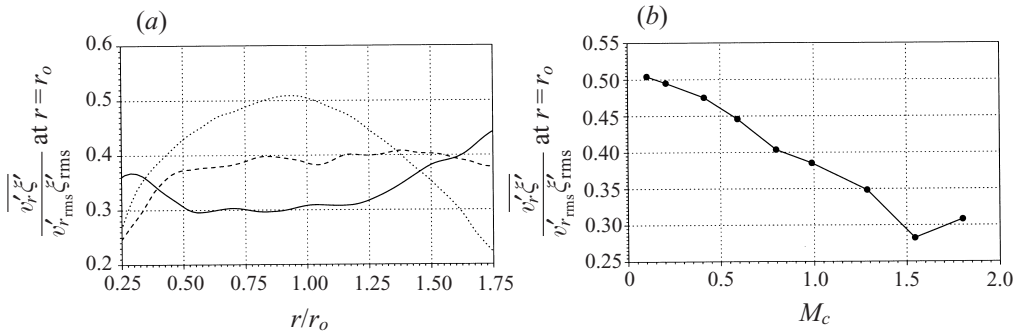


FIGURE 15. Correlation coefficient between radial velocity and scalar concentration fluctuations. (a) $\cdots\cdots$, $M_c = 0.2$; $-\cdots-$, $M_c = 0.99$; $—$, $M_c = 1.8$. (b) Correlation coefficient for all Mach number cases at $r = r_o$.

$r = r_o$. These values, which are taken as typical for each case, increase monotonically from 0.65 at the lowest Mach number to 0.97 at the highest Mach number.

Figure 15 shows the correlation coefficient $\overline{v'_r \xi'}/v'_{r,rms} \xi'_{rms}$. In contrast to the axial velocity, there is a clear trend of decreasing correlation with increasing compressibility. Also, unlike $\overline{v'_x \xi'}/v'_{x,rms} \xi'_{rms}$, all curves are not flat. Specifically, the $M_c = 0.2$ case has a rounded peak centred in the middle of the mixing region and decreases significantly toward the edges of the mixing layer. This may be caused by large structures which span the mixing region and increase the intermittency (see figure 4). The higher-Mach-number cases have flatter curves consistent with the suppression of these structures. Again, we take the $r = r_o$ values as typical, and plot them in figure 15(b) with the proviso that the low-Mach-number profiles are rounded whereas the higher-Mach-number cases are not. The $r = r_o$ correlation coefficient falls from 0.5 at $M_c = 0.1$ to 0.3 at $M_c = 1.8$.

For completeness, and to relate scalar transport to momentum transport, the correlation coefficient $\overline{v'_x v'_r}/v'_{x,rms} v'_{r,rms}$ is also given (figure 16). The behaviour is very similar to $\overline{v'_r \xi'}/v'_{r,rms} \xi'_{rms}$ with a similar rounded peak (figure 16a) for the lowest Mach numbers and flatter profiles at the higher Mach numbers. Although the correlation is higher in all cases than the corresponding values for $\overline{v'_r \xi'}/v'_{r,rms} \xi'_{rms}$, the decline of the $r = r_o$ values with increasing Mach number is nearly the same, dropping from 0.58 down to 0.36 (figure 16b).

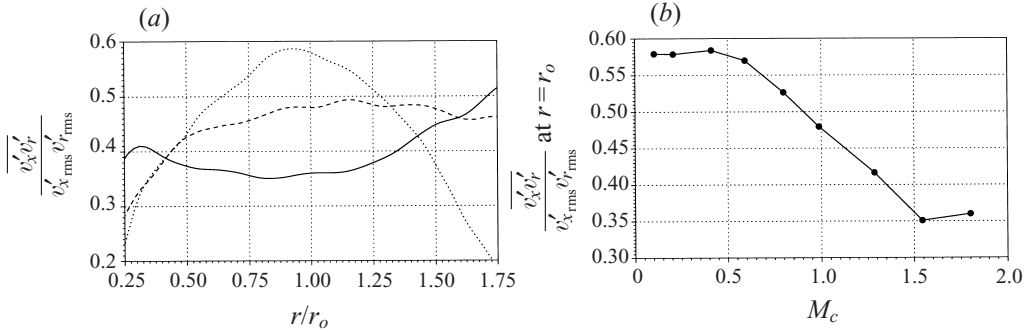


FIGURE 16. Correlation coefficient between axial and radial velocity fluctuations. (a) \cdots , $M_c = 0.2$; $---$, $M_c = 0.99$; $---$, $M_c = 1.8$. (b) Correlation coefficient for all Mach number cases at $r = r_o$.

4.7. Structure of the turbulent scalar field

To further explore the mixing process and the effect of Mach number upon it, we examine some aspects of the scalar field's structure. In particular, the large influence of compressibility upon $\overline{v'_x \xi'}/v'_{x,rms} \xi'_{rms}$ is worthy of further examination. To address this, we visualize instantaneous fluctuation fields. We focus our attention on $r = r_o$, because the values of $\overline{v'_x \xi'}/v'_{x,rms} \xi'_{rms}$ at this location are more or less typical of the mixing region. Turbulent structures in the cylindrical surface at $r = r_o$ may be examined by making contour plots of quantities on that surface and rolling them out onto a two-dimensional plane for easier viewing.

Contours of v'_x , v'_r and ξ' are shown in figure 17 for the $M_c = 0.2$ case. The v'_x and v'_r plots do not exhibit any obvious orientation of the structures. There are some regions of large perturbations and steep gradients where the jet or ambient fluid has entered the middle of the mixing region without significant change of velocity, but these are few compared to the number of such intrusions visible for the passive scalar in figure 17(c). The passive scalar field has many regions of steep gradient (indicated by clustering of contours) and large intrusions of nearly pure fluid (large uniform areas on either side of steep gradients). These patterns are almost certainly associated with the large roller structures observed at low Mach number in part 1. In figure 17, the mushroom-shaped structures discussed in §4.2 also appear, not as ejections, but as structures within the layer. They act to distort surfaces between nearly pure fluid regions which are marked by compressed contours.

At Mach number $M_c = 0.99$, all the fields have changed (figure 18). The streamwise elongation of region v'_x , v'_r and ξ' having the same sign is consistent with increased streamwise correlation lengths (Freund *et al.* 2000). The ξ' field (figure 18c) is not as dominated by clustered contours as it was at $M_c = 0.2$, and there are fewer intrusions of pure fluid. At $M_c = 0.2$ (figure 17c), it was possible to follow a single set of clustered contours across the entire azimuthal domain. This is not so at $M_c = 0.99$ (figure 18c), where the structures have shorter azimuthal extent in agreement with linear stability analyses that predict increasing obliquity at higher Mach numbers. This structural change is consistent with that observed in Part 1 where regions of low pressure were observed to become increasingly oblique with increasing Mach number. The reader is referred to that paper for a more complete discussion and visualizations of pressure fluctuations. The visual correlation between the v'_x and ξ' fields has also increased and it is now easier to identify the same structures in the two plots.

These trends continue at the highest Mach number, $M_c = 1.8$ (figure 19). The

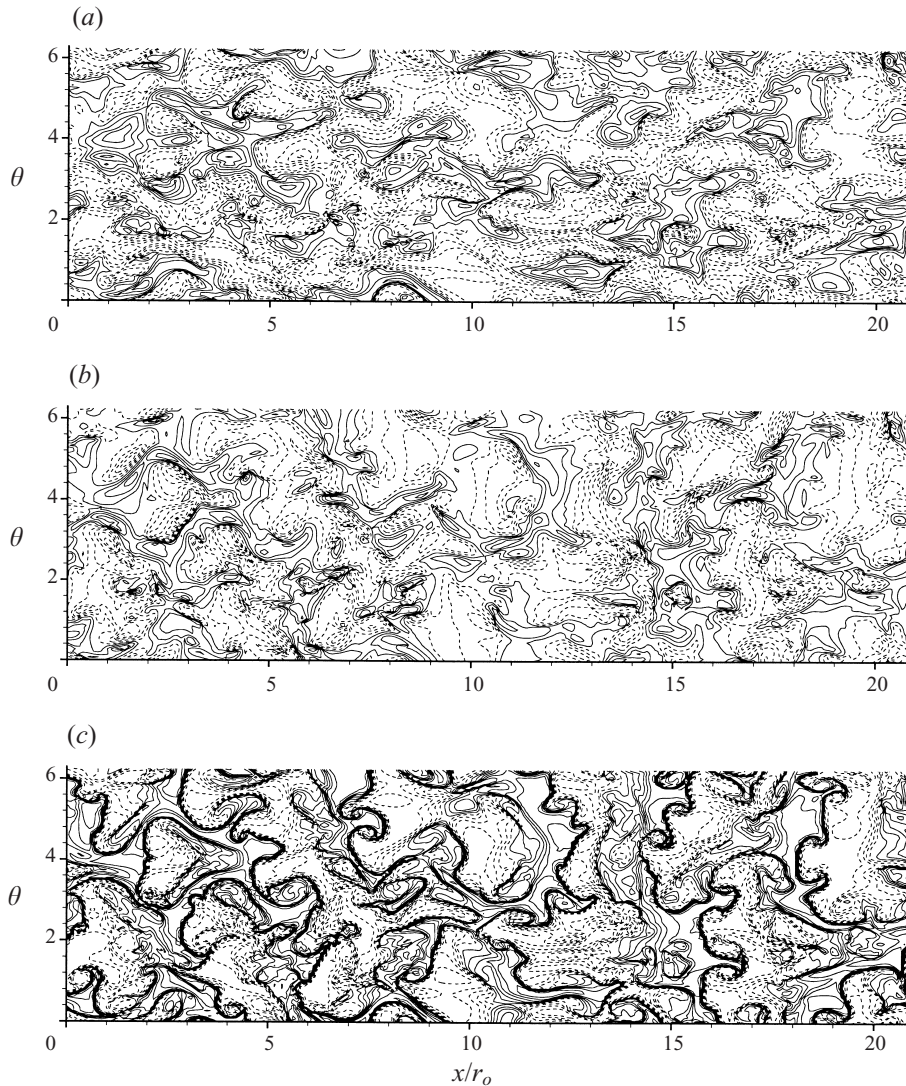


FIGURE 17. Rolled out cylindrical surfaces at $r = r_o$ for the $M_c = 0.2$ case. (a) Contours of v'_x : 12 equally spaced contours from $-0.47U_{j_0}$ to $+0.52U_{j_0}$. (b) Contours of v'_r : 12 equally spaced contours from $-0.44U_{j_0}$ to $+0.45U_{j_0}$. (c) Contours of ξ' : 12 equally spaced contours from -0.41 to $+0.49$. Positive contours are solid, negative are dashed.

streamwise extent of the structures has increased still further and the instantaneous fields of ξ' and v'_x in figure 19 are now nearly identical. The v'_r field (figure 19b), however, appears dissimilar from the other two. Regions of high v'_r do not seem to disrupt the correlation of v'_x and ξ' , also note that the intensity of v_r fluctuations decreases as M_c increases. Regions of high scalar concentration gradient are less prevalent and those remaining now have corresponding regions of high v'_x gradient. The plots in figure 19 are remarkably similar to plots of streamwise velocity and scalar concentration perturbations in the near-wall region of an incompressible turbulent channel flow (Kim & Moin 1989). The streamwise velocity–scalar correlation coefficient is also nearly unity in that flow.

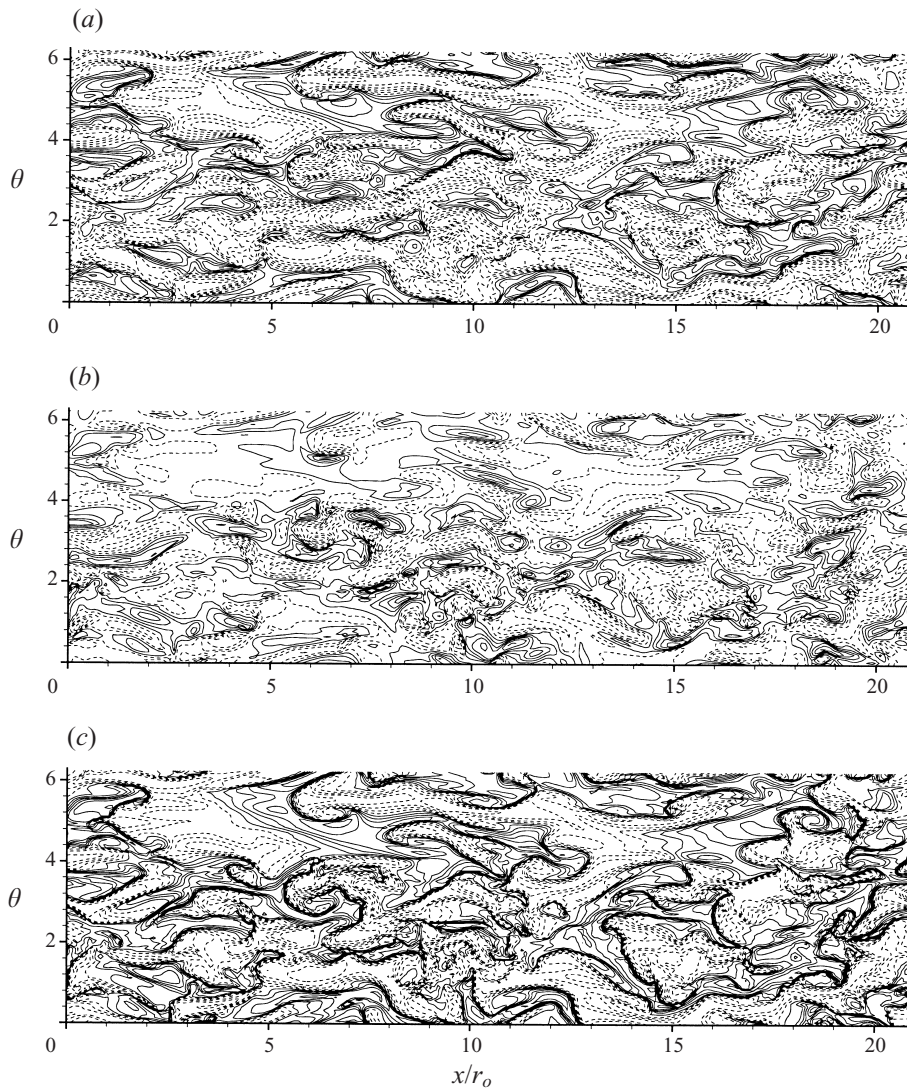


FIGURE 18. Rolled out cylindrical surfaces at $r = r_o$ for the $M_c = 0.99$ case. (a) Contours of v'_x : 12 equally spaced contours from $-0.39U_{j_0}$ to $+0.46U_{j_0}$. (b) Contours of v'_r : 12 equally spaced contours from $-0.35U_{j_0}$ to $+0.34U_{j_0}$. (c) Contours of ξ' : 12 equally spaced contours from -0.39 to $+0.50$. Positive contours are solid, negative are dashed.

The relationship between the axial velocity and scalar perturbations may be seen quantitatively in figure 20 where joint probability density functions of the fluctuations are plotted for several Mach numbers. It was not possible to converge the joint p.d.f.s into smooth plots using data from a single r location. Since ensembles are only available for the $M_c = 0.21$ and $M_c = 0.99$ runs, data over the region extending from $r = 0.9r_o$ to $r = 1.1r_o$ were used to generate the plots. Using only the $r = r_o$ points produced a joint p.d.f. that was similar but jagged. For consistency, this procedure was used for all cases. At low Mach number, the joint p.d.f. is dominated by two peaks in the first and third quadrants indicating a high probability of intense events consistent with large structures moving fluid. These peaks become less significant

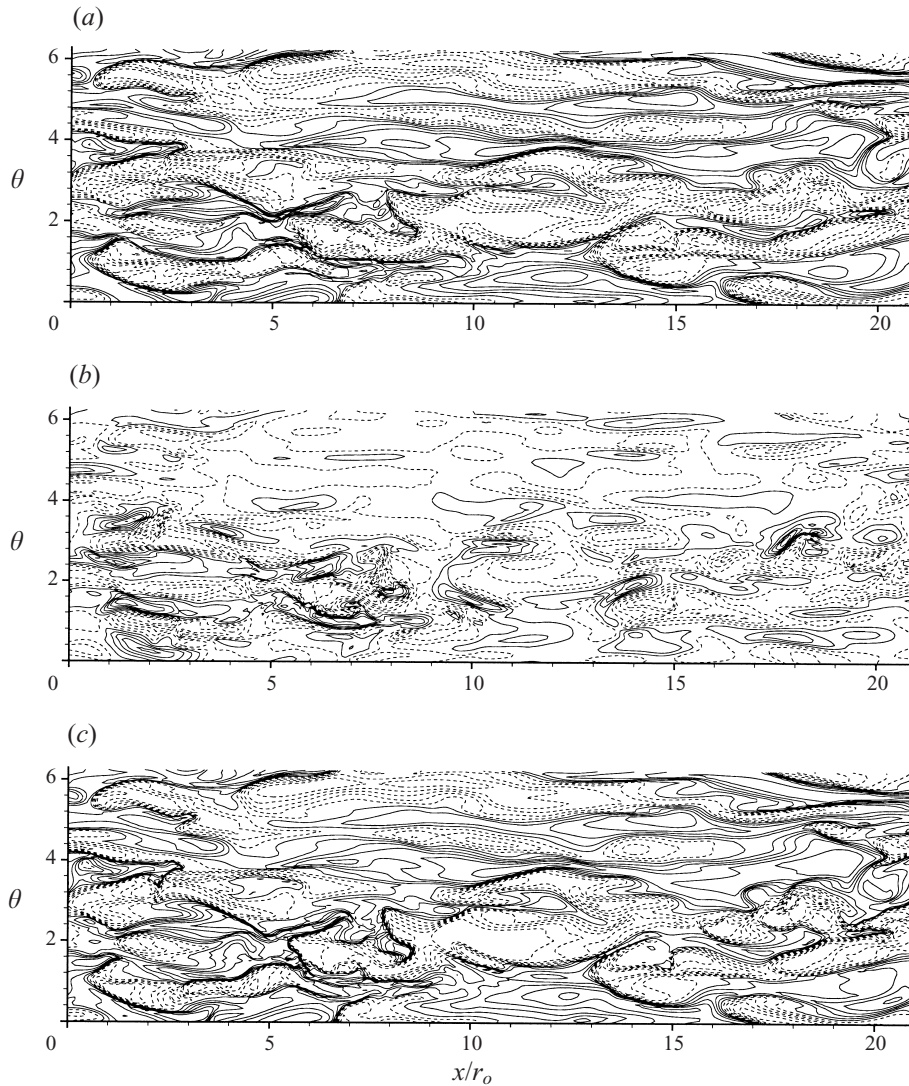


FIGURE 19. Rolled out cylindrical surfaces at $r = r_0$ for the $M_c = 1.8$ case. (a) Contours of v'_x : 12 equally spaced contours from $-0.41U_{j_0}$ to $+0.39U_{j_0}$. (b) Contours of v'_r : 12 equally spaced contours from $-0.22U_{j_0}$ to $+0.19U_{j_0}$. (c) Contours of ζ' : 12 equally spaced contours from -0.44 to $+0.43$. Positive contours are solid, negative are dashed.

as the Mach number increases and eventually the distribution falls almost onto a straight line. An exactly straight line would indicate perfect correlation.

Joint p.d.f.s of radial velocity and scalar concentration were calculated in the same way and are shown in figure 21. At low Mach numbers, it has a double-peaked shape similar to the v'_x, ζ' joint p.d.f., but as the Mach number increases, it collapses into an oval region centred at the origin indicating decorrelation with scalar fluctuation variance greater than the velocity variance.

The similarity of the v'_x and ζ' fields at high Mach number is due to the suppressed role of the pressure gradient term in the x -momentum equation. The equations for

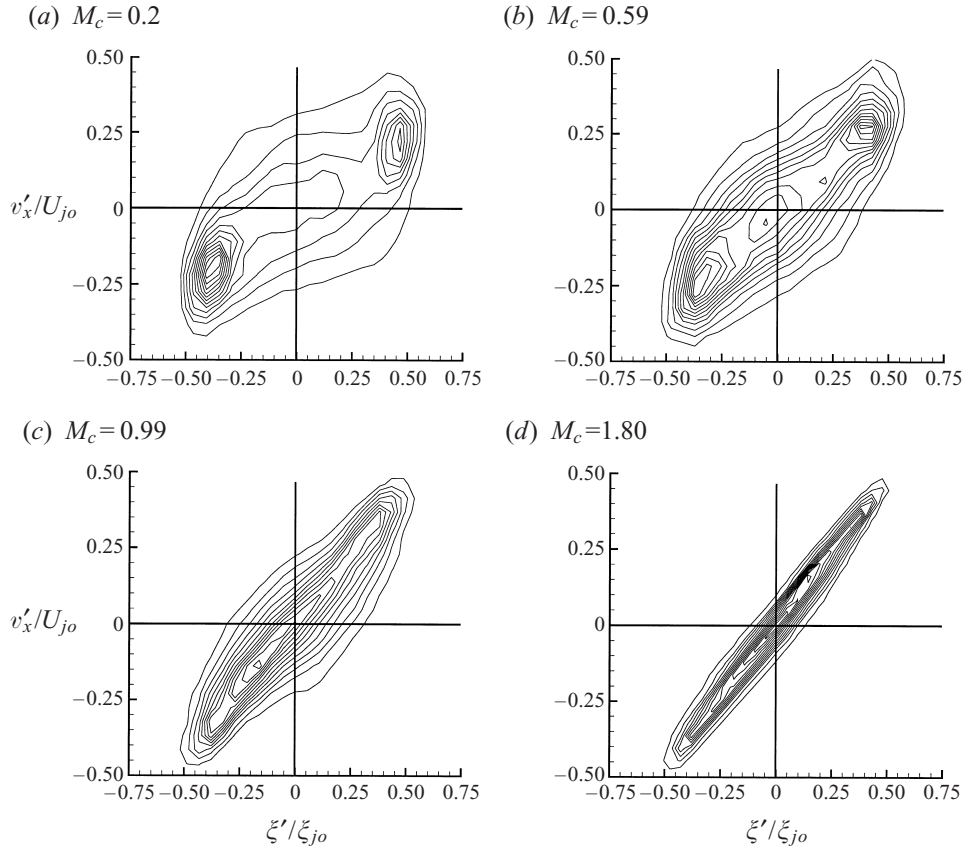


FIGURE 20. Joint probability density functions of axial velocity perturbation and passive scalar concentration perturbation. All cases have equally spaced contours from 0 to a maximum of: (a) 0.0205; (b) 0.0118; (c) 0.0165; (d) 0.0268.

ρv_x and $\rho \xi$ are

$$\frac{\partial}{\partial t}(\rho v_x) + \frac{\partial}{\partial x}(\rho v_x v_x) + \frac{1}{r} \frac{\partial}{\partial r}(r \rho v_x v_r) + \frac{1}{r} \frac{\partial}{\partial \theta}(\rho v_x v_\theta) = -\frac{\partial p}{\partial x} + V_x, \quad (4.5)$$

$$\frac{\partial}{\partial t}(\rho \xi) + \frac{\partial}{\partial x}(\rho \xi v_x) + \frac{1}{r} \frac{\partial}{\partial r}(r \rho \xi v_r) + \frac{1}{r} \frac{\partial}{\partial \theta}(\rho \xi v_\theta) = -\frac{\partial p}{\partial x} + D_\xi, \quad (4.6)$$

where D_ξ and V_x are the scalar diffusion and viscous terms, respectively. Neglecting these terms, which is reasonable since we intend to explain the behaviour of large turbulent scales, the pressure gradient in the x -momentum equation is the only difference between the two. If the pressure gradient is small and ξ and v_x have similar initial conditions, they will have a similar development. In these simulations, ξ and v_x do have similar initial conditions; they have the same mean profile and the fluctuations added to the initial v_x field are small (Freund *et al.* 2000). Figure 22 shows the relative r.m.s. contributions of the pressure and convection terms in the x -momentum equation and it is seen that the pressure gradient becomes small relative to the convection terms. This explains the surprising similarity of the ξ' and v'_x fields. A similar role of pressure was observed in incompressible channel flow, where it acts to decorrelate scalar and vorticity (Guezennec, Stretch & Kim 1990). The relative role of pressure

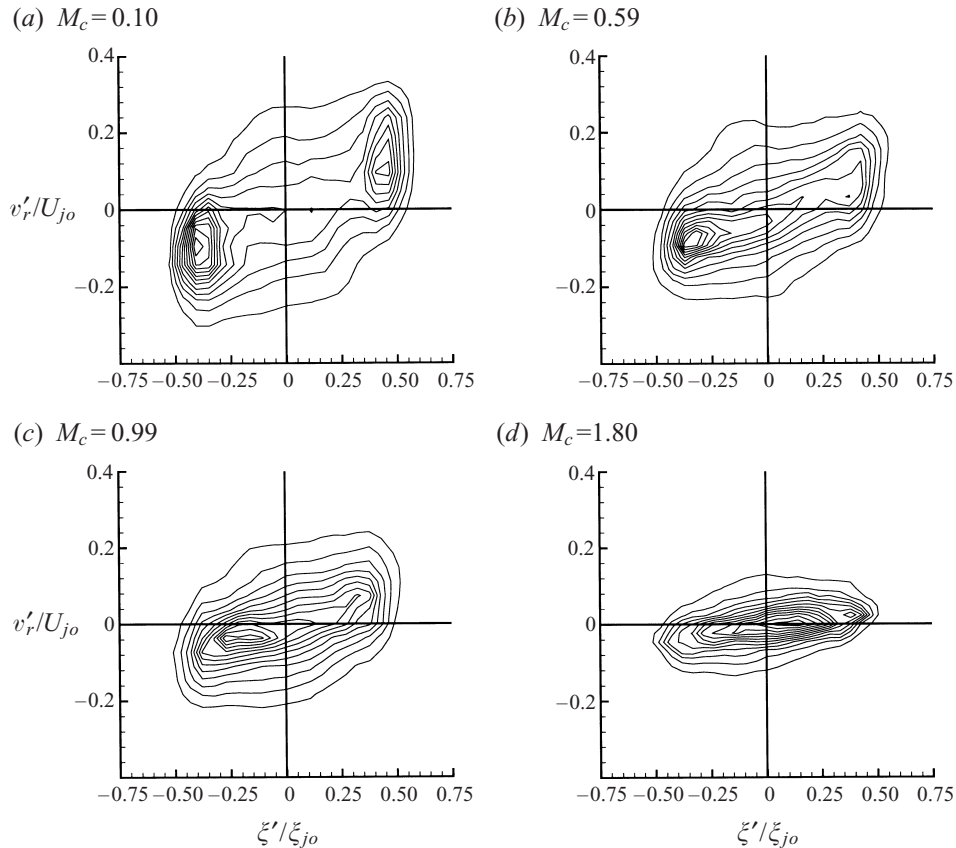


FIGURE 21. Joint probability density functions of radial velocity perturbation and passive scalar concentration perturbation. All cases have equally spaced contours from 0 to a maximum of: (a) 0.0194; (b) 0.0132; (c) 0.0162; (d) 0.0162.

in the radial momentum equation is even smaller (mostly owing to the increasing r.m.s. contribution of the sum of the convection terms), but v'_r is not expected to have scalar-like development because the initial conditions are different. The arguments presented here are also the basis of the well-known Reynolds analogy used in low-Mach-number flows. Interestingly, at high Mach numbers, pressure fluctuations are suppressed and scalar transport anisotropy increases.

5. Conclusions

A series of nine simulations at increasing convective Mach numbers ($M_c = 0.1$ to $M_c = 1.8$) were used to analyse scalar mixing in an annular free shear flow. The manner in which pure fluid is entrained into the layer was studied with probability density functions of scalar concentration. It was seen that the distributions changed from a marching type at low Mach number to non-marching at high Mach numbers, which is consistent with decreased action of large structures entraining pure fluid deep into the mixing layer. Visualization of the scalar concentration supported this interpretation and clearly showed azimuthally correlated structures driving intrusions of pure fluid into the layer. Despite these obvious changes to large-scale structure of the turbulence, it was found that the fraction of fluid in the layer that was not pure

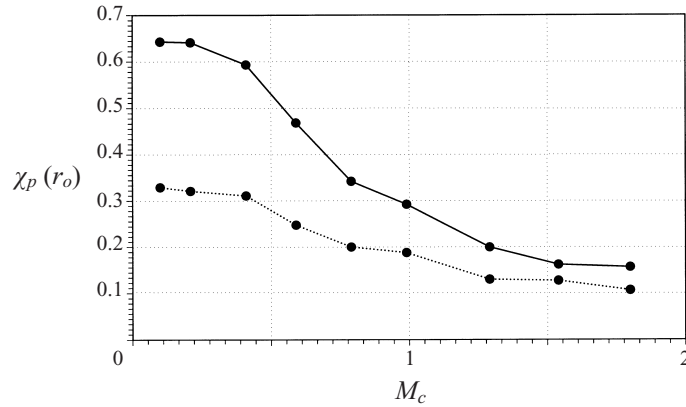


FIGURE 22. Ratio of pressure gradient term to convection terms at $r = r_o$ in: —, the axial momentum equation, $\chi_p = (\partial p / \partial x)_{\text{rms}} / ((\partial / \partial x)(\rho v_x v_x) + (1/r)(\partial / \partial r)(r \rho v_x v_r) + (1/r)(\partial / \partial \theta)(\rho v_x v_\theta))_{\text{rms}}$; and ····, the radial momentum equation $\chi_p = (\partial p / \partial r)_{\text{rms}} / ((\partial / \partial x)(\rho v_x v_r) + (1/r)(\partial / \partial r)(r \rho v_r v_r) + (1/r)(\partial / \partial \theta)(\rho v_r v_\theta) - (\rho v_\theta v_\theta / r))_{\text{rms}}$.

core or ambient fluid only increased slightly from 50% to 67% with increasing Mach number. Thus, we may conclude that the spreading rate of the layer is by far the most important factor regulating the rate at which the fluid is mixed by diffusion.

The most surprising finding was the rise of the correlation coefficient between axial velocity and scalar concentration fluctuations ($\overline{v'_x \xi'} / v'_{x,\text{rms}} \xi'_{\text{rms}}$) from 0.65 to 0.97 with increasing Mach number, while the correlation coefficient between radial velocity and concentration ($\overline{v'_r \xi'} / v'_{r,\text{rms}} \xi'_{\text{rms}}$) dropped from 0.5 to 0.3. Given this behaviour, visualizations of the scalar and axial velocity perturbation fields showed them to become nearly indistinguishable at high Mach numbers. The cause of the strong correlation between v'_x and ξ' was found to be a decrease in the relative importance of pressure gradient terms in the axial momentum equation. Hence, the large-scale axial velocity fluctuations developed principally by advection, and were therefore similar to the scalar field. The suppression of radial scalar flux scaled well with a scaling for reduced pressure fluctuations. This scaling was shown in Part 1 to explain changes in Reynolds stresses with M_c and point to the critical role of transverse turbulence lengthscale. Scalar mixing results presented here further confirm its importance and also highlight the limitations of purely scalar-based diagnostics in explaining the dynamics of the flow. Specifically, the radial correlation length of scalar fluctuations does not change much with M_c and fails to explain the compressibility effects observed in this flow.

J.B.F. acknowledges the support of the Caroline M. and Franklin P. Johnson graduate fellowship at Stanford University. Computer time was provided by CEWES, ASC, MHPCC, NAS, and ARC.

REFERENCES

- BATCHELOR, G. K. 1957 Spectrum of convected scalar quantities in turbulent fluid. Part 1. General discussion and the case of small conductivity. *J. Fluid Mech.* **5**, 113–133.
- BILGER, R. W. 1989 Turbulent diffusion flames. *Ann. Rev. Fluid Mech.* **21**, 101–135.
- BROADWELL, J. E. & BREIDENTHAL, R. E. 1982 A simple model of mixing and chemical reaction in a turbulent shear layer. *J. Fluid Mech.* **125**, 397–410.
- BROADWELL, J. E. & MUNGAL, M. G. 1991 Large-scale structures and molecular mixing. *Phys. Fluids A* **3**, 1193–1206.

- CLEMENS, N. T. & MUNGAL, M. G. 1995 Large-scale structure and entrainment in the supersonic mixing layer. *J. Fluid Mech.* **284**, 171–216.
- CLEMENS, N. T. & PAUL, P. H. 1995 Scalar measurements in compressible axisymmetric mixing layers. *Phys. Fluids* **7**, 1071–1081.
- CORRSIN, S. 1974 Limitations of gradient transport models in random walks and in turbulence. *Adv. Geophys.* **18**, 25–60.
- DAHM, W. J. A. & DIMOTAKIS, P. E. 1990 Mixing at large Schmidt number in the self-similar far field of turbulent jets. *J. Fluid Mech.* **217**, 299–330.
- DIMOTAKIS, P. E. 1991 Turbulent free shear layer mixing and combustion. *Prog. Astronaut. Aeronaut.* **137**, 265–340.
- DOWLING, D. R. 1988 Mixing in gas phase turbulent jets. PhD thesis, California Institute of Technology, Pasadena, California.
- DOWLING, D. R. & DIMOTAKIS, P. E. 1990 Similarity of the concentration field of gas-phase turbulent jets. *J. Fluid Mech.* **218**, 109–141.
- FATICA, M., VERZICCO, R. & ORLANDI, P. 1994 Rib vortices in round jets: direct and large eddy simulation. In *Application of Direct and Large Eddy Simulation to Transition and Turbulence, Chania, Crete, Greece*. CP-551, AGARD.
- FREUND, J. B., LELE, S. K. & MOIN, P. 2000 Compressibility effects in a turbulent annular mixing layer. Part 1. Turbulence and growth rate. *J. Fluid Mech.* **421**, 229–267.
- FREUND, J. B., MOIN, P. & LELE, S. K. 1997 Compressibility effects in a turbulent annular mixing layer. *Tech. Rep.* TF-72, Stanford University, Mechanical Engineering, Flow Physics and Computation Division.
- FRIELER, C. E. 1992 Mixing and reaction in the subsonic two-dimensional turbulent free shear layer. PhD thesis, California Institute of Technology, Pasadena, California.
- FRIELER, C. E. & DIMOTAKIS, P. E. 1988 Mixing and reaction at low heat release in the non-homogeneous shear layer. *AIAA Paper* 88-3626.
- GUEZENNEC, Y., STRETCH, D. & KIM, J. 1990 The structure of turbulent channel flow with passive scalar transport. *Center for Turbulence Research, Proc. of the Summer Program 1990*, pp. 127–138.
- HALL, J. L., DIMOTAKIS, P. E. & ROSEMAN, H. 1991 Some measurements of molecular mixing in compressible turbulent shear layers. *AIAA Paper* 91-1719.
- ISLAND, T. C. 1997 Quantitative scalar measurements and mixing enhancement in compressible shear layers. PhD thesis, Stanford University, Stanford, California.
- KARASSO, P. S. & MUNGAL, M. G. 1996 Scalar mixing and reaction in plane liquid shear layers. *J. Fluid Mech.* **323**, 23–63.
- KIM, J. & MOIN, P. 1989 Transport of passive scalars in a turbulent channel flow. In *Turbulent Shear Flows* **6**, pp. 85–96. Springer.
- KONRAD, J. H. 1976 An experimental investigation of mixing in two-dimensional turbulent shear flows with applications to diffusion-limited chemical reactions. PhD thesis, California Institute of Technology, Pasadena, California.
- KOCHESFAHANI, M. M. & DIMOTAKIS, P. E. 1986 Mixing in a turbulent liquid mixing layer. *J. Fluid Mech.* **170**, 83–112.
- LIEPMANN, D. & GHARIB, M. 1992 The role of streamwise vorticity in the near-field entrainment of round jets. *J. Fluid Mech.* **245**, 643–688.
- MESSERSMITH, N. L. & DUTTON, J. C. 1996 Characteristic features of large structures in compressible mixing layers. *AIAA J.* **34**, 1814–1821.
- MOIN, P., SQUIRES, K., CABOT, W. & LEE, S. 1991 A dynamic subgrid-scale model for compressible turbulence and scalar transport. *Phys. Fluids A* **3**, 2746–2757.
- MUNGAL, M. G., HERMANSON, J. C. & DIMOTAKIS, P. E. 1985 Reynolds number effects on mixing and combustion in a reacting shear layer. *AIAA J.* **23**, 1418–1423.
- PAPAMOSCHOU, D. & BUNYAJITRADULYA, A. 1997 Evolution of large eddies in compressible shear layers. *Phys. Fluids* **9**, 756–765.
- ROGERS, M. M. & MOSER, R. D. 1994 Direct simulation of a self-similar turbulent mixing layer. *Phys. Fluids* **6**, 903–923.
- SANDHAM, N. & REYNOLDS, W. 1991 Three-dimensional simulations of large eddies in the compressible mixing layer. *J. Fluid Mech.* **224**, 133–158.